A99-16403

AIAA 99-0523

A Numerical Study of Low-Reynolds-Number Separation Bubbles

Mahidhar Tatineni and Xiaolin Zhong
University of California, Los Angeles
Los Angeles, CA

37th Aerospace Sciences Meeting & Exhibit
January 11–14, 1999 / Reno, NV

A Numerical Study of Low-Reynolds-Number Separation Bubbles

Mahidhar Tatineni* and Xiaolin Zhong†
University of California, Los Angeles, California 90095

Abstract

The present study uses two dimensional numerical simulations to study unsteady low-Reynolds-number separation bubbles. The numerical study is in two parts: 1) a two dimensional time-accurate Navier-Stokes solver is used to simulate flows over the APEX airfoil, and 2) a numerical procedure is developed for localized simulations of transitional separation bubbles. The 2-D computations of flow over the APEX airfoil show that the flow is unsteady with periodic vortex shedding. A linear stability analysis of the separated flow shows that the vortex shedding is caused due to the instability of the separated flow. For transonic flows over the APEX airfoil the vortex shedding is additionally influenced by the presence of shocks. The flowfield has two characteristic time scales, one corresponding to the vortex shedding and another corresponding to the movement of the shocks. The two dimensional (2-D) airfoil simulations also showed the presence of nonlinear effects in the separated region. To better understand the characteristics of separation bubbles a numerical procedure has been developed for localized separation bubble calculations. This procedure is used to perform computations for a flat plate separation bubble test case. The separation bubble is induced by specifying a velocity gradient in the freestream. The growth of disturbances in the separation bubble is analyzed by introducing disturbances upstream of the separation bubble.

INTRODUCTION

Transitional separation bubbles are a characteristic of flows over airfoils in the low-Reynolds-number range (Re=5 $\times 10^4$ to 1 $\times 10^6$). Aerodynamic characteristics of airfoils in this flow regime are of importance in a variety of applications ranging from turbine blades to sailplanes and high altitude unmanned aerial vehicles (UAV's). [1,2] Hence, low-Reynolds-number flows with separation bubbles have been the subject of many experimental [3–7] and computational [8–16] studies. Figure 1 shows a schematic of the structure of a separation bubble. The laminar flow separates due to the adverse pressure gradient. The separated boundary layer is unstable, and there is rapid growth of disturbances. The flow consequently becomes turbulent and reattaches. The region between the separation point and the reattachment point is called the separation bubble.

The strong influence of the separation bubbles on the performance of airfoils in low-Reynolds-number flows has been shown in many experimental studies. [3,4,7] The unsteady structure of the separation bubble has been investigated in many experimental studies. The instability associated with the separated boundary layer was confirmed by Leblanc, Blackwelder, and Liebeck. [5] Their studies showed the presence of a dominant frequency in the velocity spectra in the separated region. The peak frequency was found to match the most amplified frequency calculated from linear stability theory. Dovgal, Kozlov, and Michalke [6] studied the transition process in the separation bubbles. Their results showed the initial instability of the separated flow, the linear growth of disturbances and the subsequent nonlinear interactions leading to transition.

Low-Reynolds-number flows have been numerically studied using a variety of approaches ranging from integral methods [8,12] to 2-D and 3-D direct simulations. [11,13–16] The 2-D incompressible simulations of Lin and Pauley [11] showed the unsteady nature of the flowfield and the associated vortex shedding. Our previous incompressible and compressible 2-D simulations [13,14] of flow over the APEX airfoil showed the same vortex shedding process. An analysis of the numerical results showed that the growth of disturbance waves in the separated region leads to the vortex shedding. The dominant frequency from the numerical simulations is found to agree with the most unstable frequency from a linear stability analysis. The numerical results also show the presence of nonlinear effects in the separated region. Three dimensional effects in separation bubbles for flows over a flat plate have been studied by Hildings [16] and Rist and Maucher. [15] Rist and Maucher introduced various 2-D and 3-D disturbances into the flowfield to study the nonlinear disturbance development in the separation bubble. Their simulations were able to obtain a turbulent flowfield and predicted longitudinal vortices in the reattachment region.

The present work is a continuation of our previous unsteady 2-D studies of subsonic and transonic low-Reynolds-number flows over the APEX airfoil. [13,14] The APEX airfoil was designed at NASA Dryden for

*Graduate Student, Member AIAA.
†Associate Professor, Mechanical and Aerospace Engineering Department, Member AIAA, xiaolin@seas.ucla.edu.

the planned high altitude flight tests [2] which will collect aerodynamic data in the transonic low-Reynolds-number regime. In this paper we use 2-D simulations to study the unsteady separation bubbles over airfoils and flat plates. In the transonic case there is an additional frequency associated with the movement of shocks. In addition, the presence of shocks leads to large variations in the separation location. The 2-D computations over the APEX airfoil were performed using a second order implicit Gauss-Seidel method. In addition, a numerical code is developed for localized computations of the separation bubbles using fifth order upwind schemes. [18] The code is used to compute a flat plate separation bubble test case.

OBJECTIVES

The objective of this paper is to numerically study the unsteady structure of transitional separation bubbles. The numerical approaches are as follows:

(1) Two-dimensional time-accurate computations using laminar Navier-Stokes equations for flows over airfoils. The 2-D simulations can capture the large scale unsteady structure of the separation bubbles. The flows are calculated for a range of Reynolds-numbers and Mach-numbers (subsonic and transonic). The calculations are used for a parametric study of the separation bubbles.

(2) The stability of the separated boundary layer is analyzed using a linear stability analysis and the results compared with the numerical results.

(3) The growth of disturbances in the separation bubbles is studied in greater detail by considering a flat plate test case. A separation bubble is formed by specifying a velocity gradient in the freestream. The growth of disturbances in the separation bubble is studied numerically.

NUMERICAL METHODS

Two Dimensional Computations Over Airfoils

Governing Equations

The mass, momentum and energy conservation equations for compressible flows in two dimensions are as follows :

$$\frac{\partial U}{\partial t} + \frac{\partial F}{\partial x} + \frac{\partial G}{\partial y} = 0 \tag{1}$$

where

$$\mathbf{U} = \begin{bmatrix} \rho \\ \rho u \\ \rho v \\ e \end{bmatrix} \tag{2}$$

$$\mathbf{F} = \begin{bmatrix} \rho u \\ \rho u^2 + p + \sigma_{11} \\ \rho uv + \sigma_{12} \\ u(e + p + \sigma_{11}) + \sigma_{12} v + q_1 \end{bmatrix} \tag{3}$$

$$\mathbf{G} = \begin{bmatrix} \rho v \\ \rho uv + \sigma_{21} \\ \rho v^2 + p + \sigma_{22} \\ v(e + p + \sigma_{22}) + \sigma_{21} u + q_2 \end{bmatrix} \tag{4}$$

where σ_{ij} represents the shear stresses and q_1, q_2 are the heat conduction fluxes. The equation of state is as follows:

$$p = (\gamma - 1)\left[e - \frac{1}{2}\rho\left(u^2 + v^2\right)\right] \tag{5}$$

Numerical Method

In the computations the equations are transformed from the Cartesian coordinates(x,y,t) into the curvilinear computational coordinates(ξ,η,τ). The computations are performed on a C-grid (for airfoil computations). The grids are generated using an elliptic grid generator. An implicit second order finite volume line Gauss-Seidel iteration method [17] is used for the computations. The inviscid terms are computed using the flux splitting method and central differencing is used for the viscous terms. The computation involves calculations which are implicit in the η (normal) direction, while the ξ (streamwise) direction terms are computed by a line Gauss-Seidel iteration with alternating sweeps in the backward and forward ξ directions. The computations are first order accurate in time, with the time step being small enough to resolve the time dependence of the solution. For laminar-turbulent calculations the turbulence model is used after the transition location. The transition location is determined using the transition model.

Localized Separation Bubble Calculations

Governing Equations

The governing equations are the unsteady three-dimensional Navier-Stokes equations:

$$\frac{\partial U}{\partial t} + \frac{\partial F_j}{\partial x_j} + \frac{\partial F_{vj}}{\partial x_j} = 0 \tag{6}$$

where

$$U = \{\rho,\ \rho u_1,\ \rho u_2,\ \rho u_3,\ e\} \tag{7}$$

$$F_j = \begin{Bmatrix} \rho u_j \\ \rho u_1 u_j + p\delta_{1j} \\ \rho u_2 u_j + p\delta_{2j} \\ \rho u_3 u_j + p\delta_{3j} \\ (e + p)\, u_j \end{Bmatrix} \tag{8}$$

$$F_{vj} = \begin{Bmatrix} 0 \\ \tau_{1j} \\ \tau_{2j} \\ \tau_{3j} \\ \tau_{jk}u_k - q_j \end{Bmatrix} \quad (9)$$

$$p = \rho RT \quad (10)$$

$$e = \rho(c_v T + \frac{\rho}{2} u_k u_k) \quad (11)$$

$$\tau_{ij} = -\mu\left(\frac{\partial u_i}{\partial x_j} + \frac{\partial u_j}{\partial x_i}\right) + 2\mu/3\frac{\partial u_k}{\partial x_k}\delta_{ij} \quad (12)$$

$$q_j = -\kappa\frac{\partial T}{\partial x_j} \quad (13)$$

In the numerical simulations, the governing equation (6) are transformed into the computational domain (ξ, η, ζ, τ) as follows

$$\frac{1}{J}\frac{\partial U}{\partial \tau} + \frac{\partial E'}{\partial \xi} + \frac{\partial F'}{\partial \eta} + \frac{\partial G'}{\partial \zeta} + \frac{\partial E'_v}{\partial \xi} + \frac{\partial F'_v}{\partial \eta} + \frac{\partial G'_v}{\partial \zeta} + U\frac{\partial(\frac{1}{J})}{\partial \tau} = \frac{W}{J} \quad (14)$$

where

$$E' = \frac{F_1\xi_x + F_2\xi_y + F_3\xi_z}{J} \quad (15)$$

$$F' = \frac{F_1\eta_x + F_2\eta_y + F_3\eta_z + U\eta_t}{J} \quad (16)$$

$$G' = \frac{F_1\zeta_x + F_2\zeta_y + F_3\zeta_z}{J} \quad (17)$$

$$E'_v = \frac{F_{v1}\xi_x + F_{v2}\xi_y + F_{v3}\xi_z}{J} \quad (18)$$

$$F'_v = \frac{F_{v1}\eta_x + F_{v2}\eta_y + F_{v3}\eta_z}{J} \quad (19)$$

$$G'_v = \frac{F_{v1}\zeta_x + F_{v2}\zeta_y + F_{v3}\zeta_z}{J} \quad (20)$$

where J is the Jacobian of the coordinate transformation, and ξ_x, ξ_y, ξ_z, η_x, η_y, η_z, η_t, ζ_x, ζ_y, and ζ_z are the grid transformation metrics.

The governing equations are discretized in the uniform computational space. In the equations, the transformed inviscid fluxes E', F', and G' are standard flux terms with known eigenvalues and eigenvectors. The transport flux terms E'_v, F'_v, and G'_v contain first-order spatial derivatives of velocity and temperature. These derivatives in the Cartesian coordinates (x, y, z) are transformed into the computational coordinates (ξ, η, ζ) using a chain rule for spatial discretization.

Numerical Method

The governing equation (14) is discretized in the computational domain (ξ, η, ζ, τ) using the method of lines. The equations are discretized in space using high-order finite difference methods. [18] The inviscid and viscous flux terms are discretized using different methods: central difference schemes for the viscous flux terms and upwind schemes for the inviscid flux terms. The detailed expression for the fifth order explicit upwind scheme is as follows:

$$u'_i = \frac{1}{h\, b_i}\sum_{k=-3}^{3} a_{i+k}\, u_{i+k} - \frac{\alpha}{6!\, b_i}h^5\left(\frac{\partial u^6}{\partial^6 x}\right)_i + \cdots \quad (21)$$

where

$$\begin{aligned} a_{i\pm3} &= \pm 1 + \tfrac{1}{12}\alpha \\ a_{i\pm2} &= \mp 9 - \tfrac{1}{2}\alpha \\ a_{i\pm1} &= \pm 45 + \tfrac{5}{4}\alpha \\ a_i &= 0 - \tfrac{5}{3}\alpha \qquad b_i = 60 \end{aligned}$$

These 7-3-1-0 schemes are fifth-order upwind scheme when $\alpha < 0$, and they are sixth-order central scheme when $\alpha = 0$.

For the inviscid flux vector in the governing equation (14), the flux Jacobians contains both positive and negative eigenvalues in general. A simple local Lax-Friedrichs scheme is used to split the inviscid flux vectors into positive and negative wave fields. For example, the flux term E' in Eq. (14) is split as follows:

$$E' = E'_+ + E'_- \quad (22)$$

where

$$E'_+ = \frac{1}{2}(E' + \lambda U) \quad (23)$$

$$E'_- = \frac{1}{2}(E' - \lambda U) \quad (24)$$

(25)

where λ is chosen to be larger than the local maximum eigenvalues of E':

$$\lambda = \frac{|\nabla\xi|}{J}\left(\sqrt{(\epsilon c)^2 + u'^2} + c\right) \quad (26)$$

where

$$u' = \frac{\xi_x u + \xi_y v + \xi_z w + \xi_t}{|\nabla\xi|} \quad (27)$$

The parameter ϵ is a small positive constant added for the smoothness of the splitting. The flux E'_+ and E'_- contain only positive and negative eigenvalues respectively. Therefore, in the spatial discretization of Eq. (14), the flux derivatives are split into two terms

$$\frac{\partial E'}{\partial \xi} = \frac{\partial E'_+}{\partial \xi} + \frac{\partial E'_-}{\partial \xi} \quad (28)$$

where the first term on the right hand side is discretized by an upwind high-order finite-difference method and the second term is discretized by a downwind high-order finite-difference method.

For the compressible Navier-Stokes equations (14) in a conservation-law form, the second-order derivatives do not appear explicitly in the equations. Instead, they appear as first-order derivatives in the transport flux vectors in Eq. (9). For such equations, the transport terms can be discretized by applying central finite-difference operators for the first derivative twice. [18] The approximation of the first-order derivative for computing the viscous terms is done using a sixth order central explicit scheme ($\alpha = 0$ in equation 21).

The spatial discretization of the governing equations leads to a system of first-order ordinary differential equations for the flow variables. The equations are solved using a third order low-storage Runge-Kutta scheme. [19]

Numerical Procedure

The mean flow for the localized simulations is obtained by prescribing inlet and freestream conditions from the 2-D simulations, and the time averaged 2-D mean flow as the initial conditions. For the flat plate separation bubble test case the initial condition is set to the boundary layer solution. The separation bubble is obtained by prescribing a velocity gradient in the freestream. For the unsteady calculations the disturbances are introduced upstream of the separation bubble and allowed to grow spatially through the domain. The disturbance is introduced in two ways: 1) the unsteady disturbance flow conditions are specified at the inlet based on eigenfunctions obtained through a linear stability analysis, and 2) a blowing and suction strip upstream of the separation bubble. For the flat plate separation bubble test case method (1) is used. No slip boundary conditions are used at the wall. Nonreflective boundary conditions are used in the freestream and at the exit.

RESULTS

The 2-D Navier-Stokes solver was validated by computing flow over the Eppler 387 airfoil. [13] The solver is then used to compute unsteady subsonic and transonic low-Reynolds-number flows over the APEX airfoil. The subsonic calculations showed the unsteady nature of the flow, with periodic vortex shedding. [13,14] The transonic computations show a similar vortex shedding process, with additional effects due to the presence of shocks. To better understand the characteristics of separation bubbles a flat plate test case is calculated. The separation bubble is induced by specifying a velocity gradient in the freestream. A steady separation bubble is obtained. The unsteady characteristics are studied by introducing disturbances upstream of the separation bubble. The details of the numerical results are presented below.

2-D Simulations Over the APEX Airfoil

Two-dimensional Navier-Stokes simulations are used to study laminar flows over the APEX airfoil. The calculations are performed for Mach numbers of 0.5 and 0.65, a range of Reynolds-numbers from 200 to 200,000, and a range of angles of attack from 0° to 4°. The results of the study are presented below.

Effects of Reynolds-Number Variation

The effects of Reynolds-number variation are studied by computing flows at a Mach number of 0.5, an angle of attack of 4°, and Reynolds-numbers of 200, 1000, 20000, and 200000. A section of the 434 × 75 grid used for the computations is shown in Fig. 2. The computations show that for the $Re = 200$ case the solution is steady with no separation. The streamlines for this case (Fig. 3) show that the flow remains attached. Figure 4 shows the streamlines for the $Re = 1000$ case. The figure shows that the flow separates on the upper surface of the airfoil. However, the solution is steady. When the Reynolds-number is further increased the separated flow becomes unsteady (for Re=20000 and Re=200000). In addition periodic vortex shedding is observed. This vortex shedding process is visualized in Fig. 5 using flowfield streamline plots in sequence, corresponding to one time period. Hence, the nature of the separated flow strongly depends on the Reynolds-number.

Effects of Mach Number Variation

The effects of Mach number variation are studied by performing calculations for subsonic ($M = 0.5$) and transonic ($M = 0.65$) Mach numbers. The Reynolds-number is set at 2×10^5 and the angle of attack at 4°. The unsteady computations are carried out till a periodic state is reached.

The computations show that the flow is unsteady, with vortex shedding. The vortex shedding process for the subsonic case is visualized in Fig. 5 using flowfield streamline plots in sequence, corresponding to one time period. The frequency and wavenumber corresponding to the most unstable disturbance wave are compared with the dominant frequency and wavenumber from the numerical results in Table 1. The frequency (ω_R) and wavenumber(α) are nondimensionalized as $\alpha^* = \alpha c$, $\omega_R^* = \omega_R \frac{c}{U_\infty}$. The numerical results show good agreement with the linear stability results. Detailed results for this case are given in our earlier paper. [14]

The transonic computations over the APEX airfoil were performed for the following flow conditions: $Re_\infty = 2 \times 10^5$, $\alpha = 4°$, and $M_\infty = 0.65$. Two grid sizes of 602 × 150 and 802 × 150 were used for the computations. A section of the 802 × 150 grid (over 8 processors) used for the computations is shown in Fig. 6. The results show the presence of vortex shedding as in

the subsonic case. This is illustrated in Fig. 7 which shows the unsteady variation of flowfield pressure contours calculated using the 602×150 grid. The large scale features were found to be grid independent as seen in Fig. 8, which shows the unsteady variation of flowfield pressure contours from the fine grid results. In addition to the vortex shedding, the movement of shocks on the upper surface can be seen. The unsteady nature of the flowfield can also been seen from the unsteady surface pressure variations as shown in Fig. 9. The movement of the shock leads to a much larger variation in the separation location than in the subsonic case. Also, in this case there are two dominant frequencies, one corresponding to the vortex shedding and another corresponding to the shock movement. The dominant frequencies from the computations are grid independent as shown in Table 2.

Effects of Angle of Attack Variation

The numerical simulations were done for angles of attack of 0°, 2°, and 4° for a flow at $M = 0.65$ and $Re = 200000$. Numerical results from all the cases show vortex shedding and unsteady shock movement. Figure 10 shows instantaneous pressure contours for the α=0° case. The figure shows that there is separation on both the top and bottom surface of the airfoil. On the top surface the presence of shocks can also be seen. As the angle of attack is increased the extent of separation on the lower surface is reduced as seen from Figs. 11 and 12 which show the instantaneous pressure contours for α=2° and α=4° cases respectively. In addition, the numerical simulations also show that the range of shock movement increases as the angle of attack is increased.

Flat Plate Calculations

Validation Case

The high order scheme is validated by computing a flat plate boundary layer flow. The test case considered is at a Mach number of 0.5 and the inlet Reynolds-number based on the boundary layer thickness ($Re_\delta = \frac{U_\infty \delta}{\nu}$) is 750. The 180×111 grid used for the computations is shown in Fig. 13. The disturbance flow values, corresponding to the most unstable mode, are obtained from a linear stability analysis and specified at the inlet. The disturbance quantities are obtained as follows:

$$q(y) = Re(\tilde{q}(y)e^{-i\omega t}) \tag{29}$$

where $q = (u', v', T', p')$, and $\tilde{q}$ are the corresponding eigenfunctions obtained from a linear stability analysis. The disturbance frequency is ω. For the test case chosen the nondimensional frequency ω^* ($=\frac{\omega\delta}{U_\infty}$) is 0.048. The flow is allowed to develop spatially through the domain. The numerical results obtained are compared with results from a spatial linear stability analysis. Figures 14 and 15 show the comparison of disturbance horizontal velocity eigenfunction at two locations on the flat plate. The results from the numerical simulations are in agreement with the linear stability results. The disturbance normal velocity eigenfunctions are also in good agreement as seen in Figs. 16 and 17.

Separation Bubble Case

The validated high order code is used to compute separation bubbles over a flat plate. The freestream Mach number is 0.5 and the inlet Reynolds-number based on the boundary layer thickness ($Re_\delta = \frac{U_\infty \delta}{\nu}$) is 750. The length of the domain is $480\delta_{inlet}$ and the height is $100\delta_{inlet}$. A velocity gradient ($\frac{\partial u}{\partial x}$) is specified from $150\delta_{inlet}$ to $210\delta_{inlet}$ as follows:

$$\frac{\partial u}{\partial x} = -0.16875\frac{(s-1)^2 U_\infty}{x_2 - x_1}, \tag{30}$$

where

$$s = \frac{2x - (x_1 + x_2)}{x_2 - x_1}, \tag{31}$$

where $x_1 = x_o + 150\delta_{inlet}$, $x_2 = x_o + 210\delta_{inlet}$ and x_o is the x-coordinate of the inlet location. This gradient induces a separation bubble on the flat plate. Figure 18 shows the streamlines for the mean flow. The separation bubble can be seen. Fig. 19 shows the variation of velocity in the separated region. The presence of an inflection point can be seen. The mean flow is used for unsteady calculations in which the disturbance eigenfunctions corresponding to the most unstable boundary layer mode are specified at the inlet. The disturbance is allowed to grow spatially through the domain. The calculations for this case are in progress.

SUMMARY

Unsteady low-Reynolds-number separation bubbles have been studied using 2-D time-accurate simulations. A parametric study was conducted for flow over the APEX airfoil. The 2-D computations of flow over the APEX airfoil show the unsteady periodic vortex shedding associated with the separation bubbles. The numerical results are found to agree with a linear stability analysis of the separated boundary layer. In the transonic case there are additional effects associated with the presence of shocks. There is periodic movement of the shocks leading to a corresponding movement in the separation location. A numerical procedure has been developed for localized simulations of separation bubbles. A flat plate separation bubble case is simulated using this procedure. The separation bubble is formed by prescribing a velocity gradient in the freestream. Disturbances are introduced upstream of the separation bubble. Future work will be focused on nonlinear and 3-D interactions of disturbances. In addition, the

numerical procedure used for the flat plate separation bubble simulations will be used for localized simulations of flow over airfoils.

Acknowledgments

This research has been supported by NASA Dryden Flight Research Center under Grant NCC 2-374.

References

[1] Lissman, P., "Low Reynolds Number Airfoils," *Annual Review of Fluid Mechanics*, 1983, pp. 223–239.

[2] Murray, J., Moes, T., Norlin, K., Bauer, J., Geenen, R., Moulton, B., and Hoang., S., "Piloted Simulation Study of a Balloon-Assisted Deployment of an Aircraft at High Altitude," NASA-TM 104245, 1992.

[3] Mueller, T., "Low Reynolds Number Vehicles," AGARD-AG 288, 1985.

[4] Mueller, T. and Batill, S., "Experimental Studies of Separation on Two-Dimensional Airfoils at Low Reynolds Numbers," *AIAA Journal*, Vol. 20(4), 1982, pp. 457–463.

[5] Leblanc, P., Blackwelder, R., and Liebeck., R., "A Comparison between Boundary Layer Measurements in a Laminar Separation Bubble Flow and Linear Stability Theory Calculations," *Low Reynolds Number Aerodynamics: Proceedings of the Conference*, Notre Dame, IN., June 5-7, 1989. Springer-Verlag, 1989.

[6] Dovgal, A. V., Kozlov, V. V., and Michalke, A., "Laminar Boundary Layer Separation:Instability and Associated Phenomena," *Progress of Aerospace Sciences*, Vol. 30, 1994, pp. 61–94.

[7] McGhee, R., Walker, B., and Millard, B., "Experimental Results for the Eppler387 Airfoil at Low Reynolds Numbers in the Langley Low-Turbulence Pressure Tunnel," NASA TM4062, 1988.

[8] Drela, M. and Giles., M., "Viscous-Inviscid Analysis of Transonic and Low Reynolds Number Airfoils," *AIAA Journal*, Vol. 25, 1987, pp. 1347–1355.

[9] Schneider, J. and Ewald., B., "Integration of Linear Stability Methods into Navier-Stokes Solvers for Computation of Transonic Laminar Airfoils," AIAA Paper 94-1849-CP, 1994.

[10] Vatsa, V. and Carter, J., "Analysis of Airfoil Leading-Edge Separation Bubbles," *AIAA Journal*, Vol. 22(12), 1984, pp. 1697–1704.

[11] Lin, J. M. and Pauley, L. L., "Low-Reynolds-Number Separation on an Airfoil," *AIAA Journal*, Vol. 34(8), 1996, pp. 1570–1577.

[12] Drela, M., "Transonic Low-Reynolds-Number Airfoils," *Journal of Aircraft*, Vol. 29(6), 1992, pp. 1106–1113.

[13] Tatineni, M. and Zhong, X., "Numerical Simulation of Unsteady Low-Reynolds-Number Separated Flows Over Airfoils," AIAA Paper 97-1929, 1997.

[14] Tatineni, M. and Zhong, X., "Numerical Simulations of Unsteady Low-Reynolds-Number Separated Flows Over the APEX Airfoil," AIAA Paper 98-0412, 1998.

[15] Rist, U. and Maucher, U., "Direct Numerical Simulation of 2-D and 3-D Instability Waves in a Laminar Separation Bubble," *AGARD-CP-551*, 1994.

[16] Hildings, C., "Simulation of Laminar and Transitional Separation Bubbles," *Technical Reports from Royal Institute of Technology, Sweden*, Technical Report 1997:19, 1997.

[17] MacCormack, R., "Current Status of Numerical Solution of the Navier Stokes Equations," AIAA Paper 85-0032, 1985.

[18] Zhong, X., "Direct Numerical Simulation of Hypersonic Boundary-Layer Transition Over Blunt Leading Edges, Part I:New Numerical Methods and Validation," AIAA Paper 97-0755, Jan. 1997.

[19] Williamson, J. H., "Low-Storage Runge-Kutta Schemes," *Journal of Computational Physics*, Vol.35, pp. 48-56, 1980.

[20] Moin, P., Squires, K., Cabot, W., and Lee, S., "A dynamic subgrid-scale model for compressible turbulence and scalar transport," *Physics of Fluids A*, Vol.3(11), Nov. 1991.

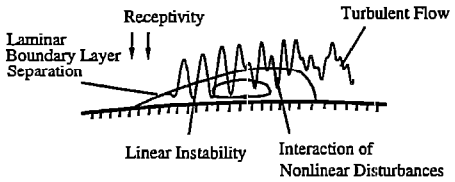

Figure 1: **Structure of the separation bubble for low-Reynolds-number flows. A schematic detailing the growth of disturbances in various regions of the separation bubble.**

	LST	Numerical Solution	% Error
α^*	62.51	66.32	6
ω_R^*	31.39	28.7	8.5

Table 1:Comparison of numerical results with the linear stability theory (LST). $\omega_R^* = \omega_R \frac{c}{U_\infty}$ **is the nondimensional frequency and** $\alpha^* = \alpha c$ **is the nondimensional wavenumber. Flow over the APEX airfoil at** $M_\infty = 0.5$, $Re_\infty = 2 \times 10^5$ **and** $\alpha = 4°$.

	Coarse Grid	Fine Grid	% difference
f_s	100.3 Hz	104.6 Hz	4
f_v	778.7 Hz	806.5 Hz	3.5

Table 2:Comparison of shock movement frequency and the vortex shedding frequency from computations of different grid sizes. f_s **is shock movement frequency and** f_v **is the vortex shedding frequency. Flow over the APEX airfoil at** $M_\infty = 0.65$, $Re_\infty = 2 \times 10^5$ **and** $\alpha = 4°$.

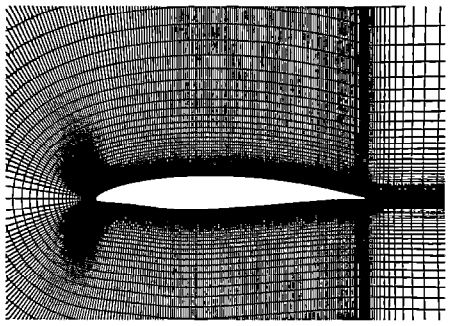

Figure 2: **A section of the 434 x 75 grid used for calculations of flow over the APEX airfoil.**

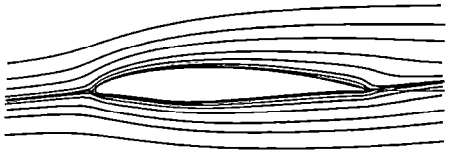

Figure 3: **Flowfield streamline contours showing fully unseparated flow over the APEX airfoil for** $M = 0.5$, $\alpha = 4°$ **, and** $Re = 200$. **Flow is steady in this case.**

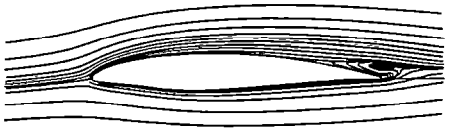

Figure 4: **Flowfield streamline contours showing separated flow over the APEX airfoil for** $M = 0.5$, $\alpha = 4°$ **, and** $Re = 1000$. **The separated flow is steady in this case.**

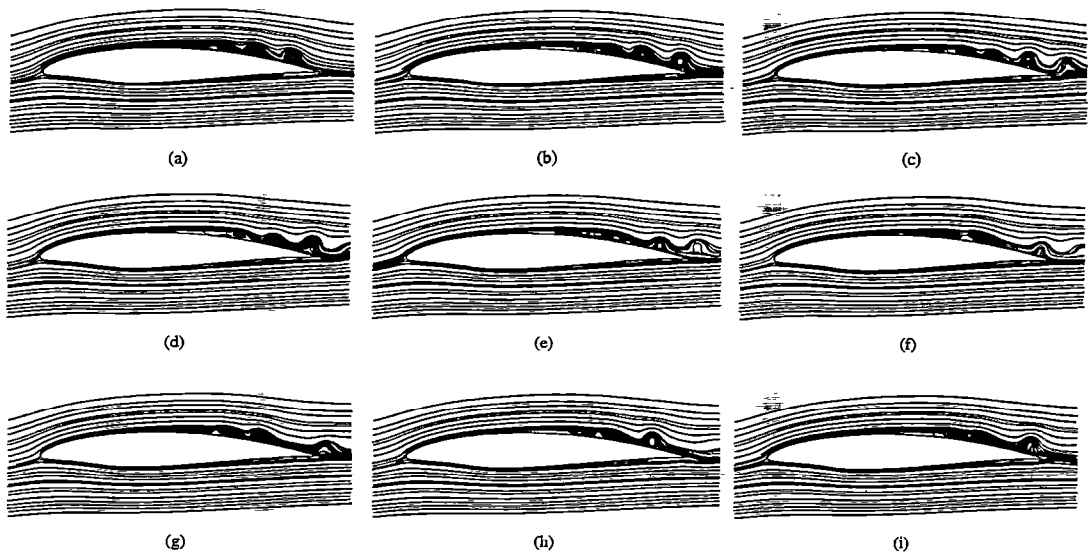

Figure 5: **Flowfield streamline plots (a)-(i) in sequence, corresponding to one time period, showing the vortex shedding process. Flow over the APEX airfoil at $M_\infty = 0.5$, $Re_\infty = 2 \times 10^5$, and $\alpha = 4°$ Computations using a 410 x 75 grid.**

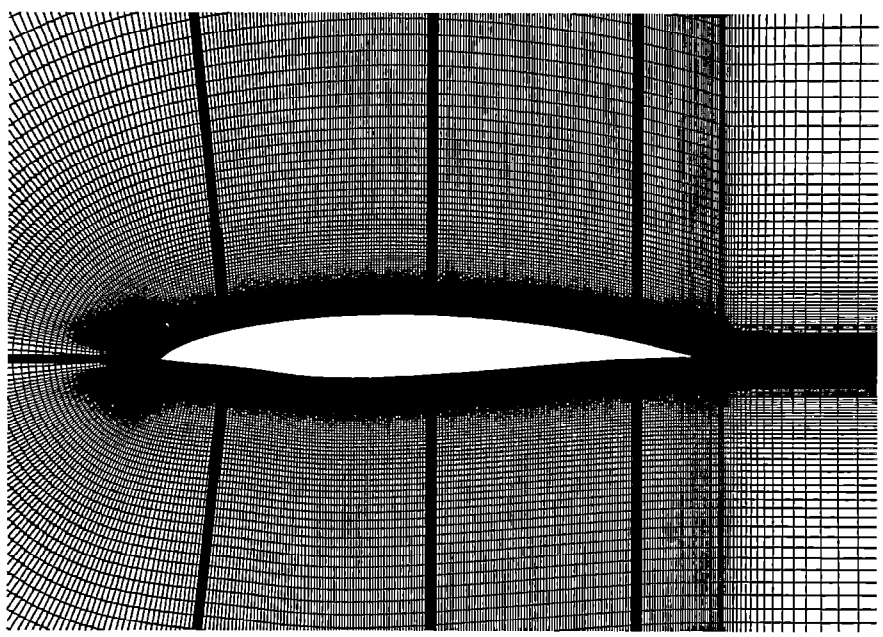

Figure 6: **A section of the 802 x 150 grid (distributed over 8 processors) used for the computations over the APEX airfoil.**

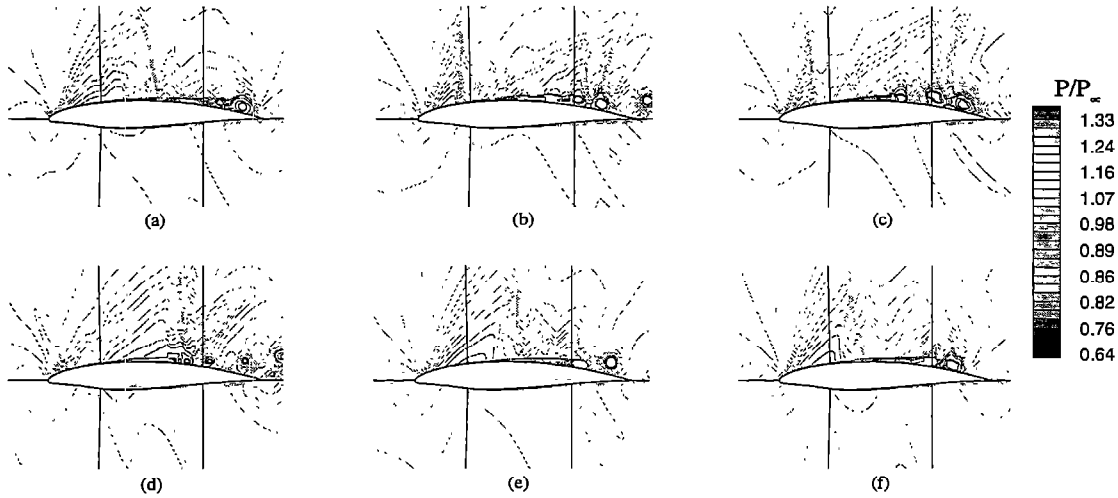

Figure 7: **Unsteady variation of flowfield pressure contours for transonic flow over the APEX airfoil at $M_\infty = 0.65$, $Re_\infty = 2 \times 10^5$, and $\alpha = 4°$. Computations using a 602×150 grid. The movement of the shocks on the upper surface of the airfoil can be seen.**

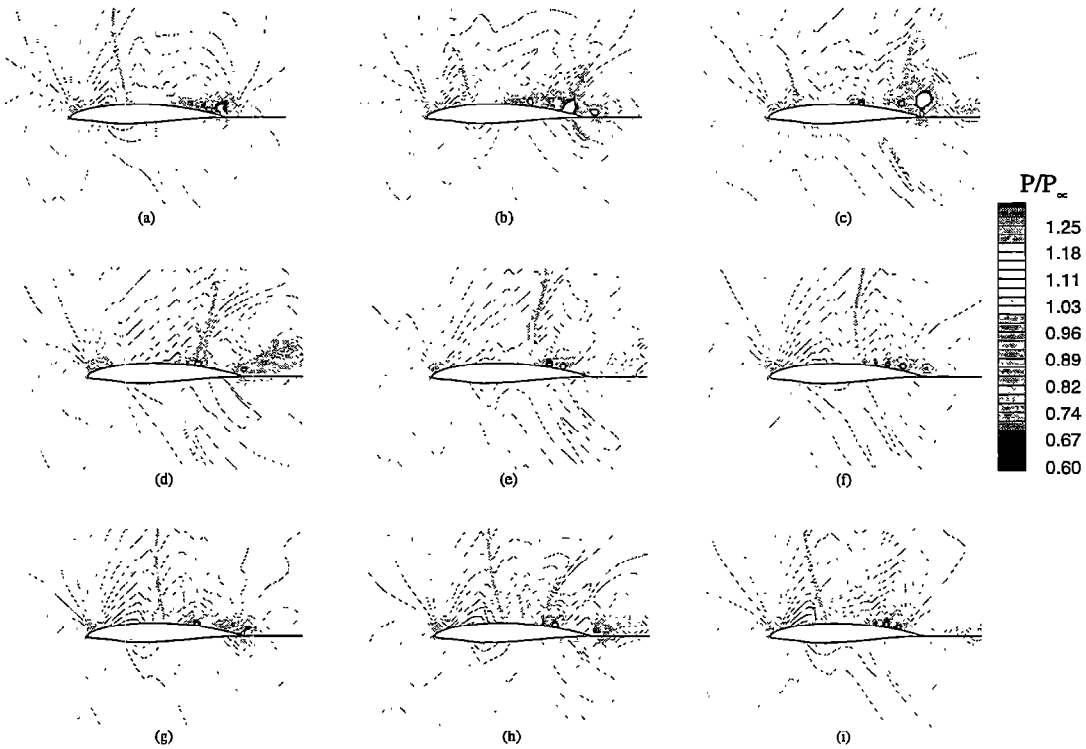

Figure 8: **Unsteady variation of flowfield pressure contours, (a)-(i) in sequence in time for transonic flow over the APEX airfoil at $M_\infty = 0.65$, $Re_\infty = 2 \times 10^5$, and $\alpha = 4°$. Computations using a 802×150 grid. The fine grid results also show the complex shock movement and vortex shedding process. The large scale structures are found to be grid independent.**

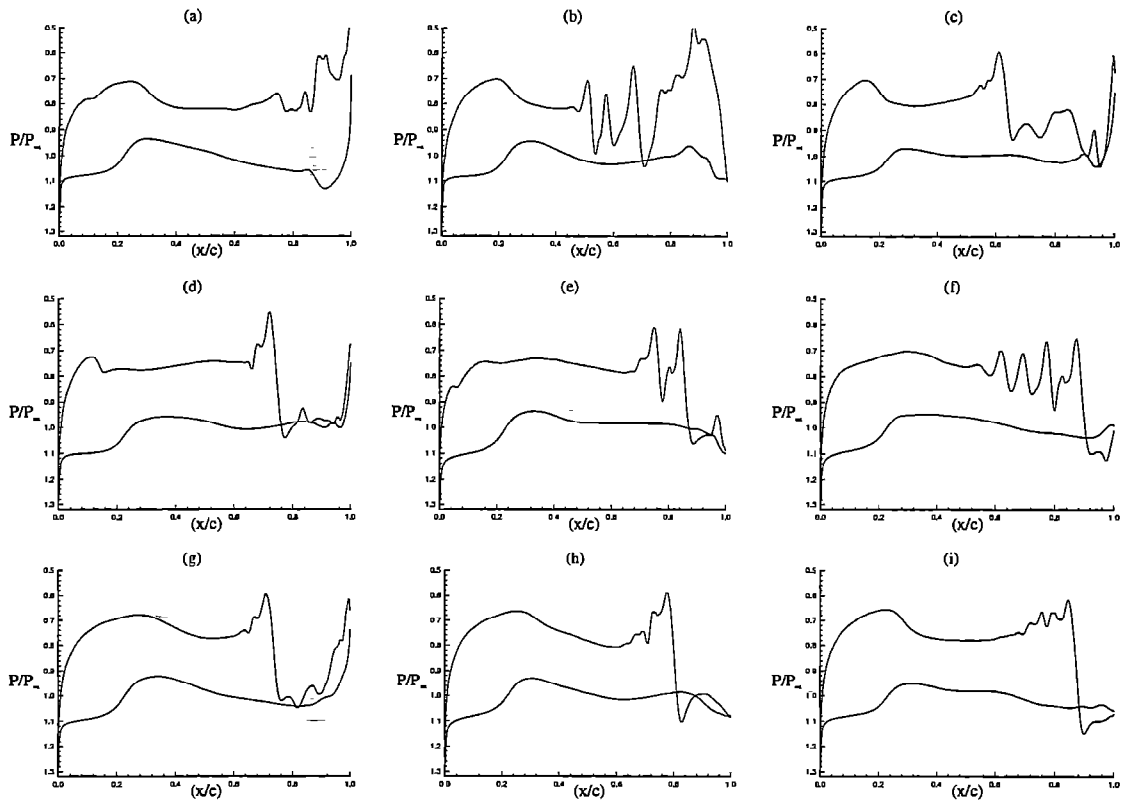

Figure 9: **Unsteady variation of surface pressure, (a)-(i) in sequence in time for transonic flow over the APEX airfoil at $M_\infty = 0.65$, $Re_\infty = 2 \times 10^5$, and $\alpha = 4^\circ$. Computations using a 802×150 grid.**

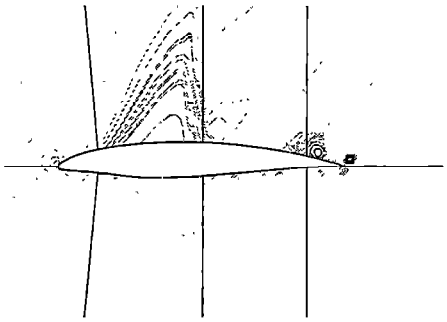

Figure 10: **Instantaneous pressure contours showing the shocks and vortex shedding. Flow over the APEX airfoil at $M_\infty = 0.65$, $Re_\infty = 2 \times 10^5$, and $\alpha = 0°$ Computations using a 802 x 150 grid over eight processors.**

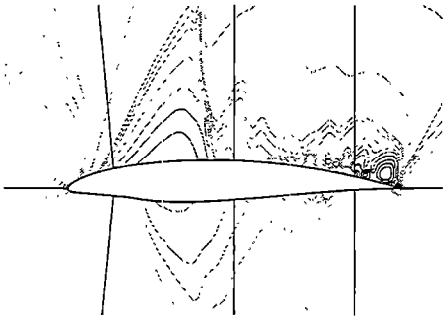

Figure 11: **Instantaneous pressure contours showing the shocks and vortex shedding. Flow over the APEX airfoil at $M_\infty = 0.65$, $Re_\infty = 2 \times 10^5$, and $\alpha = 2°$ Computations using a 802 x 150 grid over eight processors.**

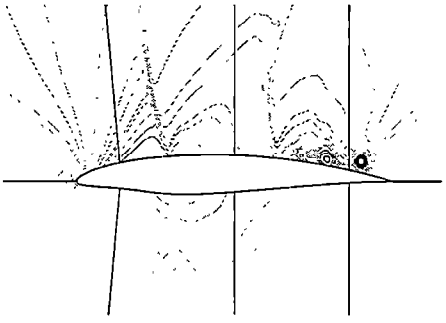

Figure 12: **Instantaneous pressure contours showing the shocks and vortex shedding. Flow over the APEX airfoil at $M_\infty = 0.65$, $Re_\infty = 2 \times 10^5$, and $\alpha = 4°$ Computations using a 802 x 150 grid over eight processors.**

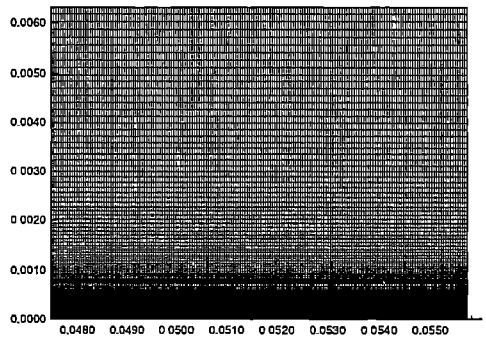

Figure 13: **The 180 x 111 grid used for the flat plate boundary layer test case.**

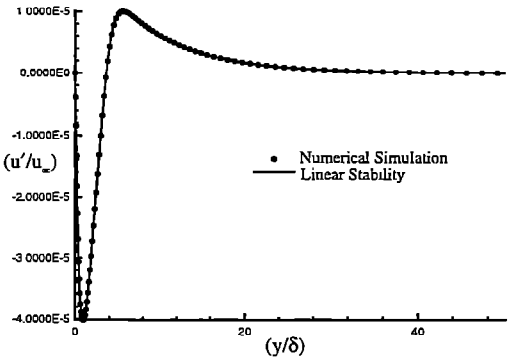

Figure 14: **Comparison of numerical simulation and linear stability results for disturbance-u eigenfunction.**

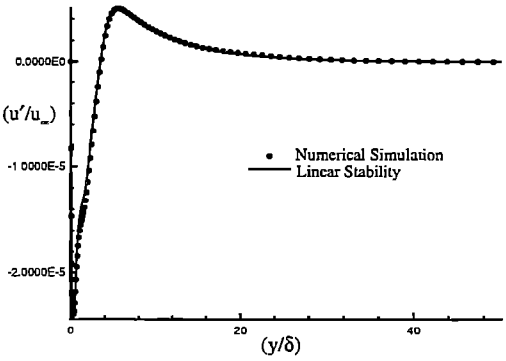

Figure 15: **Comparison of numerical simulation and linear stability results for disturbance-u eigenfunction.**

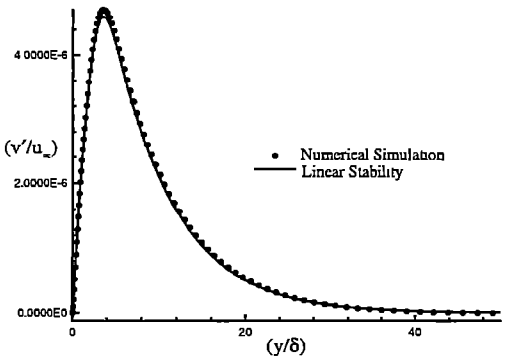

Figure 16: **Comparison of numerical simulation and linear stability results for disturbance-v eigenfunction.**

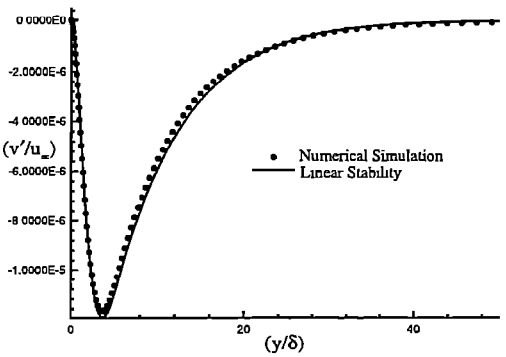

Figure 17: **Comparison of numerical simulation and linear stability results for disturbance-v eigenfunction.**

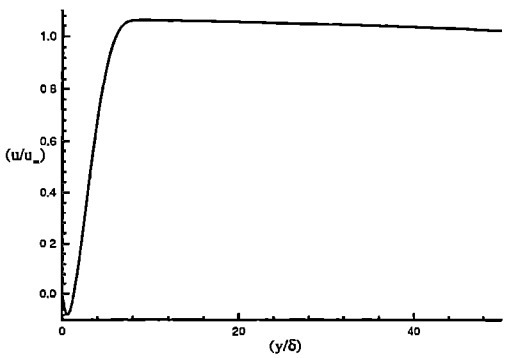

Figure 19: **Variation of horizontal velocity at a station in the separated region. Mean flow for flat plate separation bubble test case.**

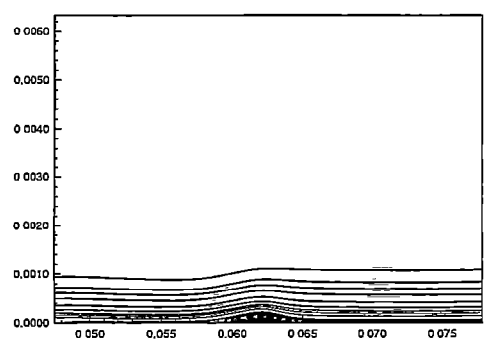

Figure 18: **Mean flow streamlines showing the separation bubble over a flat plate. The separation bubble is induced using a velocity gradient in the freestream.**